

# PLUMENet: Efficient 3D Object Detection from Stereo Images

Yan Wang<sup>3</sup> Bin Yang<sup>1,2</sup> Rui Hu<sup>1</sup> Ming Liang<sup>1</sup> Raquel Urtasun<sup>1,2</sup>

**Abstract**—3D object detection is a key component of many robotic applications such as self-driving vehicles. While many approaches rely on expensive 3D sensors such as LiDAR to produce accurate 3D estimates, methods that exploit stereo cameras have recently shown promising results at a lower cost. Existing approaches tackle this problem in two steps: first depth estimation from stereo images is performed to produce a pseudo LiDAR point cloud, which is then used as input to a 3D object detector. However, this approach is suboptimal due to the representation mismatch, as the two tasks are optimized in two different metric spaces. In this paper we propose a model that unifies these two tasks and performs them in the same metric space. Specifically, we directly construct a *pseudo LiDAR feature volume (PLUME)* in 3D space, which is then used to solve both depth estimation and object detection tasks. Our approach achieves state-of-the-art performance with much faster inference times when compared to existing methods on the challenging KITTI benchmark [1].

## I. INTRODUCTION

Self-driving vehicles have the potential to revolutionize the future of mobility. In order to build a robust and safe autonomy system, reliable real-time perception is a necessity. Many self-driving cars are equipped with expensive LiDAR sensors, which provide accurate depth measurements that facilitate reasoning in 3D metric space. In recent years LiDAR based 3D detectors [2]–[6] have shown very promising results. However, LiDAR sensors remain costly and have limited range, limiting their applicability.

On the other hand, cameras are cheaper and much more accessible than LiDAR. Even when LiDAR is available, cameras can improve the robustness of perception [11] as they provide high-resolution texture information. A major disadvantage of cameras is the difficulty of 3D reasoning. Some approaches [12], [13] use image features to regress 3D bounding boxes. However, as images are distorted representations of 3D information, reasoning in image space makes it hard to achieve precise 3D localization. Pseudo-LiDAR-based approaches [14] first estimate depth from images and then transform the predicted depth image into 3D points (mimicking LiDAR), which can be processed by a standard 3D detector. The performance of pseudo-LiDAR directly depends on the quality of the estimated depth. Stereo images provide disparity cues that enable better depth estimation compared to monocular images. Recent stereo based pseudo-LiDAR models [10], [14], [15] have greatly reduced the performance gap between camera and LiDAR based 3D

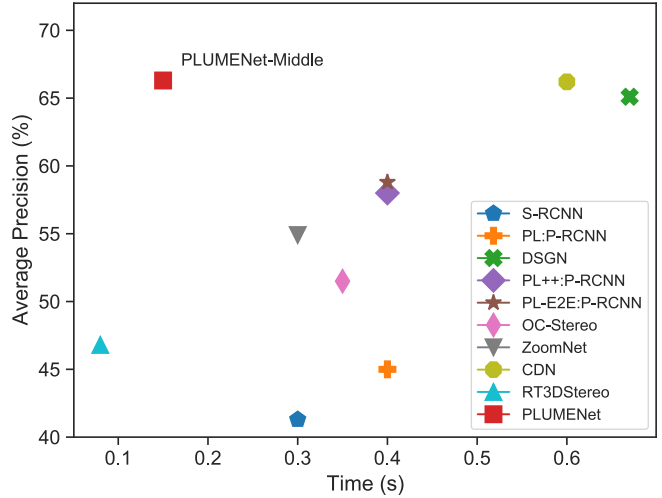


Fig. 1. **Inference Time vs. Average Precision** on KITTI [1] testing set. We report the average precision (AP) in bird’s eye view (BEV) at moderate level. Our PLUMENet-Middle achieves state-of-the-art 66.3% AP while running at 6.6 Hz.

detectors. These models usually construct the cost volume in image coordinate space with disparity or depth as the third dimension. Matching costs are computed for all voxels and depth is then estimated by taking the local minimum along the third dimension (*i.e.*, disparity or depth).

Although stereo based 3D detection models have shown promising results, they have several shortcomings. First, learning the 3D cost volume in image space is very costly in memory and computation due to the image’s high resolution and the extra dimension required for the features. The typical processing time for one frame is 0.5 seconds [9], [16], which is prohibitive in a safety critical application such as self-driving, where reaction time is key for collision avoidance. Second, depth estimation is performed in image space while the downstream detection is performed in 3D space. Due to perspective projection, nearby objects occupy many more pixels than faraway objects. This imbalance may lead to biased depth estimation with degraded long-range detection performance. This distortion effect is clearly shown in Fig. 2, where we visualize the feature volumes in image space and 3D metric space respectively.

To overcome the two aforementioned problems, in this paper we directly construct a *pseudo LiDAR feature volume (PLUME)* in 3D metric space from which we perform both depth estimation and 3D object detection. As a result, we can build PLUME to leverage the full resolution image features. This contrasts with existing methods that have to heavily downsample image-centric features to keep memory

<sup>1</sup>Waabi.

<sup>2</sup>University of Toronto. Correspondence: yw763@cornell.edu, byang@cs.toronto.edu, urtasun@cs.toronto.edu

<sup>3</sup>Cornell University.

\*This work was done by all authors while at Uber ATG.

TABLE I  
COMPARISONS OF DIFFERENT 3D FEATURE VOLUME (FV) REPRESENTATIONS.

	Disparity FV	Depth FV	Pseudo-LiDAR FV	LiDAR FV
<b>References</b>	[7], [8]	[9], [10]	Ours	[3]
<b>Data density</b>	dense	dense	dense	sparse
<b>Depth distribution</b>	distorted under perspective projection	distorted under perspective projection	uniform	precise but sparse
<b>Metric space</b>	image space	image space	3D/BEV space	3D/BEV space
<b>Feature extraction</b>	3D convolution	3D convolution	3D/2D convolution	3D/2D convolution

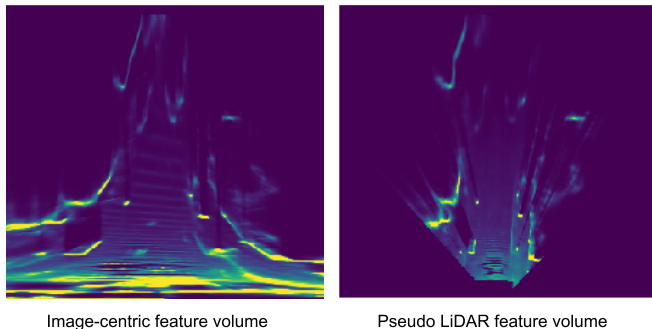


Fig. 2. Feature volumes in image space and 3D metric space.

and computation costs reasonable. Thus, our approach allows for greater efficiency while enabling superior detection performance. Furthermore, with our formulation, 3D occupancy directly supervises the depth estimation model, thereby avoiding the imbalance issue that image-based metrics create.

We compare the effectiveness of our approach on the challenging KITTI benchmark [17]. As shown in Fig. 1, our model achieves 66.3% average precision (AP) at moderate level on the testing set, surpassing all previously published methods that do not use external training data. Importantly, the inference time of our model is only 150 milliseconds, which is  $4 \times$  faster than other high-accuracy detectors [9], [15].

## II. RELATED WORK

*a) Stereo Depth Estimation:* Estimating depth from stereo images has been extensively investigated. The fundamental principle is to create correspondences between the left and right images. Existing depth estimation pipelines typically consists of four steps [18]: (1) Computing the matching cost of image or feature patches over a range of disparities; (2) Regularizing and smoothing the matching cost via aggregation; (3) Inspecting the low-cost regions to estimate disparities; (4) Applying post-processing to refine the disparity results. Deep neural networks have been exploited as part of this pipeline. [19] uses a convolutional network to compute the matching cost followed by non-learned based cost aggregation and disparity refinement. [20] further improves the performance and efficiency of this approach by using an efficient Siamese network. [8] utilized a 3D disparity feature volume in image space, dimensions of which are image height  $\times$  image width  $\times$  disparity. Then a 3D convolutional network is applied to the feature volume for cost aggregation. Since the depth is inversely

proportional to disparity, a small disparity represents a large depth. [10] argues that using the disparity feature volume will over-optimize the close-range depth and introduces a depth feature volume that replaces the disparity with depth. This design change allows the model to directly output depth. [15] proposes a new loss function based on the Wasserstein distance to further improve the depth prediction on object boundaries.

*b) LiDAR-based 3D Object Detection:* LiDAR sensors capture high quality depth measurements and facilitate many 3D reasoning tasks. LiDAR based 3D detectors are extensively used by self-driving vehicles to perform accurate 3D perception. These methods can be divided into two categories, depending on the LiDAR point encoding utilized. Voxelization-based methods [2], [3], [11], [21]–[23] divide the 3D space into voxels, which are represented by learned or hand-crafted features on 3D points. Then 3D or bird’s eye view (BEV) convolution can be applied to extract 3D features used by the detection header. The second category of methods utilize graph operators to directly process the points [24]–[26]. The features and connections are directly computed from the point coordinates and the spatial proximity of points. Different from 3D and BEV convolution, point based operations make use of the sparsity of points and produce per-point output features. These two types of representations make the trade-off between efficient computation (with better locality of data structure) and precise information (without discretization error). Recently fusion based approaches [6], [27] have been proposed to combine them together.

*c) Image-based 3D Object Detection:* Early works utilized a 2D frontal-view (monocular image) detection pipeline [28]–[30], however, the 3D detection performance lags far behind LiDAR-based solutions [12], [13], [31]–[39]. This gap has been significantly narrowed by pseudo-LiDAR based approaches [14], which instead of directly predicting the 3D bounding boxes from monocular images, first estimate depth at each pixel. Then the camera pose is used to un-project the pixels into 3D space to produce the pseudo-LiDAR representation. After that, standard LiDAR-based 3D detectors can be applied on the pseudo-LiDAR. OC-Stereo [40], CG-stereo [16] and disp-RCNN [41] add auxiliary 2D bounding box regression or instance segmentation tasks to help distinguish the background from foreground pixels. PL-E2E [42] proposed an end-to-end version of this framework where the detection loss supervises the depth network. However, as the core problem of representation mismatch is not addressed, the performance gain brought by

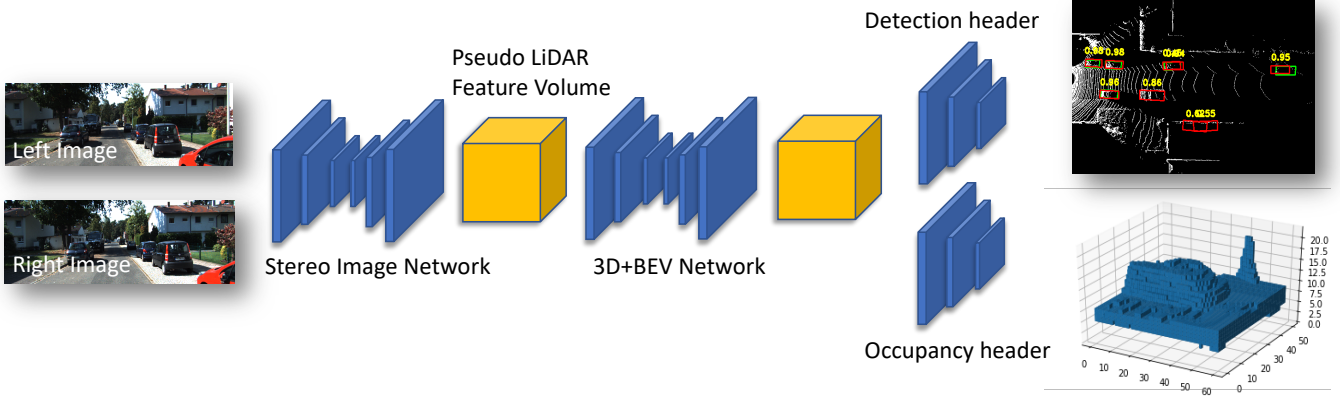


Fig. 3. **Overview of PLUMENet:** (1) stereo image network, (2) pseudo LiDAR feature volume (PLUME), (3) 3D-BEV network, (4) multi-task headers. The network takes as input a stereo pair, and outputs the reconstructed 3D scene in the form of an occupancy grid and object bounding boxes in bird’s eye view (BEV).

end-to-end learning is minimal. In contrast, in this paper we unify the representation utilized by the depth estimator and the object detector by employing a pseudo LiDAR feature volume. As a result, both tasks are optimized under the same 3D metric space, and most of the feature computation is shared, leading to a faster solution with superior detection accuracy.

Similar ideas of building 3D feature volumes directly from camera images has also been explored in previous works [9], [39], [43]. Our work differs from them in the following aspects. While [43] only focuses on 3D object reconstruction, we extend it to the full scene and optimize the representation jointly with the downstream task of 3D object detection. [39] builds the 3D feature volume from monocular images only and learns with 3D detection loss alone, while our approach exploits stereo matching cues to resolve the inherent depth ambiguity with auxiliary occupancy supervision. In [9] the same multi-task setting is explored with much worse performance, because it simply replaces the traditional image-centric feature volume as a 3D one without any network architecture change. In our work we find that traditional architecture is sub-optimal for the 3D feature volume. Specifically, the stereo image network needs to output high-resolution image features (instead of downsampled ones) so that the reconstructed 3D feature volume can capture fine details in stereo images to reason about depth especially in the long range. For the 3D convolutions used on 3D feature volume, we can also significantly improve the efficiency by replacing some of them with 2D BEV convolutions. As a result, we achieve superior detection accuracy with more than  $4\times$  speedup in model inference time.

### III. METHOD

Recent stereo-based 3D detection models have achieved remarkable progress. The top performing stereo models [10], [14]–[16], [42] follow a similar pipeline, where depth is estimated from stereo features and then the depth/features are used as points/voxels to perform 3D object detection. To

estimate the depth, all these methods construct cost volumes in the image space, with disparity as the third dimension. However, depth reasoning in image space may result in sub-optimal performance in 3D space tasks. Moreover, disparity-based cost volumes require expensive computations or rely on downsampling which results in loss of accuracy, as they are directly parameterized in terms of the image size. To overcome these issues, we propose an efficient stereo-based detector by replacing the disparity cost volume in image space with a novel *pseudo LiDAR feature volume (PLUME)* in 3D space.

Our model consists of four components: (1) A 2D convolutional network extracts multi-scale features from stereo images; (2) A pseudo LiDAR feature volume is constructed in 3D space and filled with stereo features; (3) A hybrid 3D-BEV convolutional network performs 3D reasoning; and (4) Multi-task headers predict 3D occupancy grids as well as object bounding boxes. Note that while the proposed PLUME is constructed in 3D space, we output object estimates in bird’s eye view (BEV) space, as this is what matters in the downstream tasks of self-driving (e.g., motion forecasting, motion planning). This is achieved by appending a BEV based detection header. Note however, that the occupancy estimation is performed in 3D space so that the intermediate representations preserve full 3D information. In the case of outputting 3D bounding boxes, we can simply replace the BEV detection header with a 3D based one. We refer the reader to Fig. 3 for an illustration of our model.

#### A. Stereo Image Network

We use a 2D convolutional network to extract powerful stereo image features for downstream depth estimation and 3D detection. Stereo images provide disparity cues that disambiguate the depth estimation task when compared to utilizing monocular images. Disparity here refers to the offset of two locations (obtained by projecting a 3D point onto stereo images) along the epipolar line. Since the stereo images are rectified, this search is only horizontal. Depth is inversely proportional to disparity and can be readily

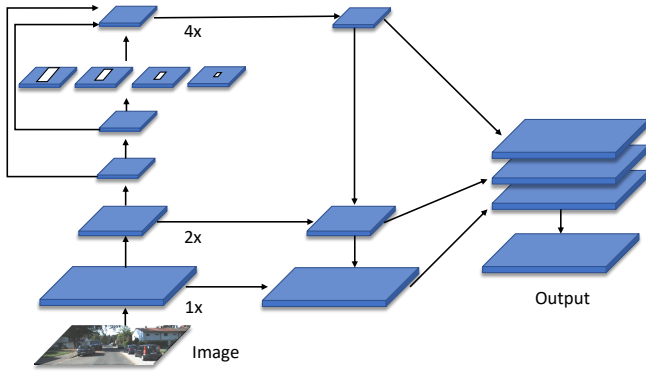


Fig. 4. The stereo image network architecture.

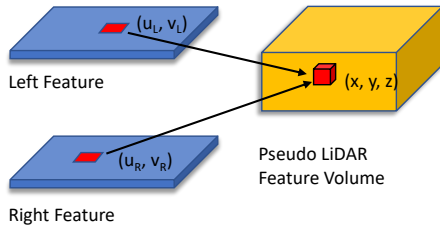


Fig. 5. Illustration of building the pseudo LiDAR feature volume (PLUME). Yellow box indicates the 3D feature volume. Blue box is 2D feature maps.

computed from it. As the precision of disparity directly depends on the image resolution, we need high-resolution image features with multi-scale context to achieve good performance. Based on this consideration we design our stereo image network. Our model uses a spatial pyramid pooling network (SPPN) [7] and a feature pyramid network (FPN) [29] to extract multi-scale features. Importantly, the finest scale in the FPN has the same resolution as the original image. We refer the reader to Fig. 4 for an illustration of the architecture.

Note that in other stereo models it is non trivial to use full resolution features. To estimate disparity, these models construct cost volumes by comparing all the stereo pixel pairs with the same vertical coordinate, where the comparison can be implemented as the correlation of two feature vectors, or as a non-linear function parameterized with neural networks (our case). The cost volume has three dimensions, image height, image width and disparity. If the original image size is used, the 3D cost volume will consume huge amounts of memory and result in costly computation. In contrast, we do not construct a disparity volume and our image feature maps are in 2D, which enable us to use full image resolution efficiently.

### B. Pseudo LiDAR Feature Volume (PLUME)

To perform depth estimation and 3D detection in the same 3D metric space, we directly construct a pseudo LiDAR feature volume. An illustration of PLUME is given in Fig. 5. Specifically, we divide the 3D space in a given range into regular 3D voxels. We assume all voxel centers can be projected onto the images, and use the projection to retrieve

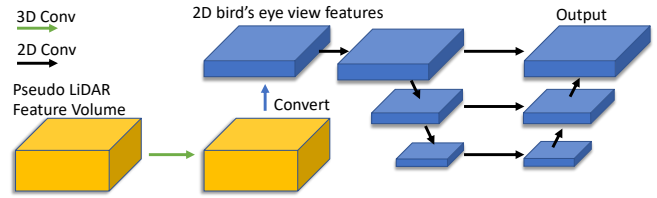


Fig. 6. The 3D-BEV network architecture. Yellow box indicates the 3D feature volume. Blue box is 2D feature maps.

the stereo image features generated by our stereo image network. The feature of each voxel is then the concatenation of retrieved image features and voxel coordinates. With the constructed feature volume, we apply additional neural network layers to classify each voxel as occupied (object surface) or not. In this way, we are performing an additional form of depth estimation. However, different from image centric cost volumes in other models, our depth estimation directly operates in 3D space. In the next section, we will describe an efficient neural architecture for PLUME.

### C. Efficient 3D-BEV Network

3D convolution is a common choice to extract features from 3D feature volumes. However, compared to 2D convolution, 3D convolution is much more costly in terms of memory and computation. For self-driving perception, the height dimension is very compact when compared to the other dimensions. For example, the maximum vehicle height rarely exceeds 5 meters, but the detection range in the other two dimensions can easily exceed 80 meters. Motivated by this fact, we propose an efficient 3D-BEV network by replacing 3D convolutions with 2D BEV convolutions. Fig. 6 shows the overall architecture of the network, which consists of two 3D convolutional layers followed by a 2D hourglass convolutional network. The first two 3D convolutional layers reason about the scene and object shapes in the height dimension as well as provide a large enough receptive field. We then convert the 3D feature volume to a 2D BEV feature map without loss of information by flattening both height and feature dimensions. A 2D hourglass convolutional network then further increases the receptive field in the horizontal and depth dimensions. In Section IV-C, we show that this hybrid design greatly improves the efficiency while achieving superior performance.

### D. Multi-Task Headers

a) *Occupancy header*: The occupancy header consists of two convolutional layers. It takes the output features of our 3D-BEV network as input, and outputs a  $D \times W$  2D feature map with  $H$  channels, where the channel dimension represents the height. We reshape this feature map to 3D occupancy voxels, and apply a sigmoid operation to generate the occupancy probability for each voxel.

b) *Detection Header*: We use an efficient single-stage object detection model based on PIXOR [3] as our detection header. This model takes the output feature map of our 3D-BEV network as input, and then predicts the bounding boxes

TABLE II

**3D OBJECT DETECTION RESULTS ON THE KITTI TEST SET. WE REPORT  $AP_{BEV}$  OF THE CAR CATEGORY, SORTED AT MODERATE LEVEL. ALL THE MODELS TAKE AS INPUT ONLY STEREO IMAGES.**

Method	easy	moderate	hard	Time (ms)
S-RCNN [45]	61.9	41.3	33.4	300
PL [14]	67.3	45.0	38.4	400
RT3DStereo [46]	58.8	46.8	38.4	<b>80</b>
OC-Stereo [40]	68.9	51.5	43.0	350
Disp-RCNN [41]	73.9	52.4	43.7	420
ZoomNet [47]	72.9	54.9	44.1	300
PL++ [10]	78.3	58.0	51.3	400
PL-E2E [42]	79.6	58.8	52.1	400
DSGN [9]	82.9	65.1	56.6	670
CDN [15]	<b>83.3</b>	66.2	<b>57.7</b>	600
PLUMENet-Middle	83.0	<b>66.3</b>	56.7	150

in BEV. It consists of a feature encoder, a feature decoder and a prediction header. The encoder has five blocks of layers. The first block has two convolutional layers with 32 channels and stride 1. The remaining blocks are composed of bottleneck residual layers [44] with number of layers 3, 6, 6, 3 respectively. The output dimension is  $16\times$  smaller than the input. The decoder is an FPN [29] with top-down pathway and lateral connections, outputting feature maps with a  $4\times$  down-sampling factor. The prediction header then takes the FPN fused feature maps and passes them through classification and regression layers to estimate the bounding box size  $(w, h)$ , BEV location  $(u, v)$  and orientation  $\theta$  at each pixel.

### E. Learning

We adopt a stage-wise multi-task learning approach. Specifically, we first train the network backbone (stereo image network and 3D-BEV network) plus the occupancy header with depth estimation loss, and then fix the backbone’s weights and train the detection header with object detection loss.

We use binary cross entropy (BCE) to compute the occupancy prediction loss. Let  $p \in (0, 1)$  be the prediction and  $y \in \{0, 1\}$  be the ground-truth occupancy of a voxel, where label 1 indicates that the voxel contains at least one LiDAR point. For each voxel, we define the *depth loss* as

$$\mathcal{L}_{\text{depth}}(p, y) = (y \log(p) + (1 - y) \log(1 - p)) \quad (1)$$

Note that we ignore all voxels outside the camera field of view.

The detection loss consists of focal loss for classification and smooth $_{\ell_1}$  loss over the bounding box regression terms: size, position and orientation:

$$\mathcal{L}_{\text{detection}} = \mathcal{L}_{\text{focal.loss}} + \mathcal{L}_{\text{smooth}_{\ell_1}} \quad (2)$$

$$\mathcal{L}_{\text{focal.loss}}(p, c) = \begin{cases} -\alpha(1-p)^\gamma \log(p) & \text{if } c = 1 \\ -(1-\alpha)p^\gamma \log(1-p) & \text{otherwise,} \end{cases} \quad (3)$$

$$\mathcal{L}_{\text{smooth}_{\ell_1}}(x) = \begin{cases} 0.5|x| & \text{if } |x| < 0.5 \\ |x| - 0.5 & \text{otherwise,} \end{cases} \quad (4)$$

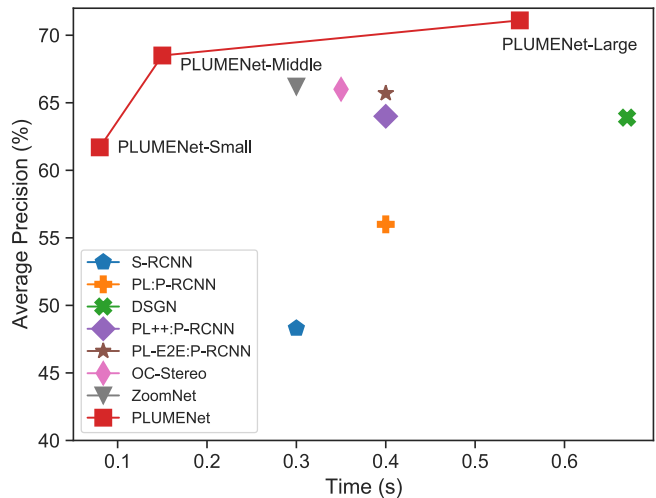


Fig. 7. **Inference Time v.s. Average Precision** on KITTI [1] validation set. We report the average precision (AP) in bird’s eye view (BEV) at moderate level. Our PLUMENet significantly outperforms other stereo-based object detectors. Specifically, PLUMENet-Middle achieves new state-of-the-art 68.4% AP while being  $2.3\times$  faster than ZoomNet [47]. PLUMENet-Large achieves 71.1% AP with a similar speed as DSGN [9].

where  $p, c$  and  $x$  are the class prediction, class label, and distance between predicted and ground-truth regression terms respectively.

## IV. EXPERIMENTS

In this section we first compare PLUMENet with state-of-the-art stereo-based BEV detection models. The results show that our approach significantly outperforms other models, while achieving  $2.3\times$  faster inference speed. We then conduct ablation studies to validate the improvements brought by full resolution image features, the hybrid 3D-BEV network and the pseudo LiDAR feature volume (PLUME). Finally, we show qualitative results of the proposed model.

### A. Experimental Setting

*a) Dataset:* We evaluate stereo-based BEV object detection on the KITTI detection benchmark [1], which contains 7,481 training and 7,518 test samples. We follow the same training and validation splits used by [32], which divides the training set to 3,712 training and 3,769 validation samples respectively.

*b) Evaluation Metric:* We focus on BEV object detection and report results on both the validation and test set. We follow prior works [9], [10], [14] and use Average Precision (AP) computed at 0.5 and 0.7 Intersection-Over-Union (IoU) as our evaluation metric. The KITTI benchmark further splits the labels into three levels: easy, moderate and hard according to the 2D bounding box height in the image, occlusion and truncation level.

*c) Training Details:* We set the PLUME range to be  $[-32, 32] \times [2, 62.8] \times [-1, 2]$  meters and the voxel resolution to be 0.2 meter. We adopt a stage-wise multi-task learning approach: we first train the model with depth loss for 50 epochs, and then train with detection loss for another 50

TABLE III

BEV OBJECT DETECTION RESULTS ON THE KITTI VALIDATION SET. WE REPORT  $AP_{BEV}$  OF THE CAR CATEGORY. ALL METHODS TAKE STEREO IMAGES AS INPUT.

Method	IoU $\geq$ 0.5			IoU $\geq$ 0.7			Time (ms)
	easy	moderate	hard	easy	moderate	hard	
3DOP [32]	55.0	41.3	34.6	12.6	9.5	7.6	-
MLF [13]	-	53.7	-	-	19.5	-	-
S-RCNN [45]	87.1	74.1	58.9	68.5	48.3	41.5	300
PL [14]	88.4	76.6	69.0	73.4	56.0	52.7	400
DSGN [9]	-	-	-	83.2	63.9	57.8	670
PL++ [10]	89.8	83.8	77.5	82.0	64.0	57.3	400
Disp-RCNN [41]	90.7	80.5	71.0	77.6	64.4	50.7	420
PL-E2E [42]	90.5	84.4	78.4	82.7	65.7	58.4	400
OC-Stereo [40]	90.0	80.6	71.1	77.7	66.0	51.2	350
ZoomNet [47]	90.6	<b>88.4</b>	71.4	78.7	66.2	57.6	300
PLUMENet-Small	87.8	80.7	75.2	74.4	61.7	55.8	<b>80</b>
PLUMENet-Middle	91.0	85.9	80.5	83.5	68.5	62.8	150
PLUMENet-Large	<b>91.3</b>	86.6	<b>81.6</b>	<b>84.7</b>	<b>71.1</b>	<b>65.1</b>	530

TABLE IV

ABLATION RESULTS ON THE KITTI VALIDATION SET. WE REPORT  $AP_{BEV}$  OF THE CAR CATEGORY.

Experiments	Method	IoU $\geq$ 0.7			Time (ms)
		easy	moderate	hard	
Image Feature Resolution	<u>Full size</u>	<b>83.5</b>	<b>68.5</b>	<b>62.8</b>	150
	Half Size	78.3	66.2	60.0	140
	Quarter Size	78.2	62.1	56.1	<b>138</b>
Feature Volume Network	<u>3D-BEV Network</u>	<b>83.5</b>	<b>68.5</b>	62.8	150
	BEV Network	75.6	62.6	56.3	<b>110</b>
	3D Network	82.2	68.2	<b>64.8</b>	230
Image Feature Fusion	<u>w/o fusion</u>	83.5	68.5	62.8	<b>150</b>
	with fusion	<b>83.9</b>	<b>68.9</b>	<b>63.4</b>	155

epochs. In the first stage we use an initial learning rate of 0.001, and decay by  $10\times$  at epochs 35 and 45 respectively. In the second stage we use an initial learning rate of 0.01 and decay at epochs 30 and 45. Our model is trained on 4 RTX5000 GPUs with a mini-batch size of 8.

### B. Experimental Results

We compare PLUMENet with state-of-the-art stereo based models on BEV object detection. The results on the validation and testing sets are summarized in Table III and Table II respectively. For a fair comparison we only compare with methods that do not exploit external data and labels. We designed three different versions of PLUMENet, namely, PLUMENet-Small, PLUMENet-Middle and PLUMENet-Large, using different network sizes by varying the number of feature channels throughout the network architecture. We evaluate the middle version on the testing set, and all three versions on the validation set. On the test set, our model achieves 66.27% moderate AP at 0.7 IoU, surpassing all previously published stereo based detectors. Importantly, our model has an inference time of 150 ms (measured on a NVIDIA Tesla V100 GPU), which is  $4\times$  faster than other high-accuracy detectors [9], [15].

On the validation set, PLUMENet-Small is a real-time prediction model, which runs in only 80ms per frame. It has competitive performance with the state-of-the-art and is more than  $3.75\times$  faster. PLUME-Middle only adds 70ms, but

outperforms all other models on both validation and test sets. For example, when IoU $\geq$ 0.7, PLUME-Middle outperforms the efficient ZoomNet [47] 4.8, 2.3 and 5.2 points on easy, moderate and hard levels respectively, while reducing the inference latency by 70%. On the test set, PLUMENet-Middle is  $4\times$  faster than comparable baselines CDN [15] and DSGN [9]. In summary, PLUMENet-Middle outperforms all baselines [9], [10], [14], [40], [42] that use image-based disparity/depth feature volume, while resulting in much faster inference. These results suggest that PLUME is an effective and efficient feature volume representation for the task of stereo based 3D detection. A detailed detection AP and inference time comparisons on the validation and test sets are summarized in Figs. 7 and 1.

### C. Ablation Study

We conduct a set of ablation studies to validate the importance of each model component. All these ablations are trained on the KITTI training set and evaluated on the validation set. We use the same learning hyper-parameters for all models. The results are shown in Table IV. We use underline to indicate the final model used to compare with other methods. In each section of the result table, we only vary one component and keep the others unchanged.

a) *Image Feature Resolution*: By default we use the full resolution features extracted from the stereo image network. To achieve the half and quarter-sized resolution (feature map



the reader to the supplementary video for more qualitative results on KITTI validation set. Fig. 9 shows the occupancy predictions of our model. PLUMENet can output high quality voxel predictions, where the objects have correct shapes and precise locations.

## V. CONCLUSION

We have proposed PLUMENet, a model that utilizes efficient pseudo LiDAR feature volume representation for stereo-based BEV object detection. PLUMENet achieves state-of-the-art results on KITTI benchmark [1] while being  $4\times$  faster than the baselines. We also propose a real-time model which makes reliable predictions in only 80 ms. Furthermore, we build a large PLUMENet model which significantly outperforms the state-of-the-art. An extensive ablation study is conducted along with qualitative comparisons to better understand the proposed method. Challenges to address in the future include adapting our approach to low-light and extreme weather conditions.

## REFERENCES

- [1] A. Geiger, P. Lenz, C. Stiller, and R. Urtasun, "Vision meets robotics: The kitti dataset," *IJRR*, 2013. 1, 5, 8
- [2] X. Chen, H. Ma, J. Wan, B. Li, and T. Xia, "Multi-view 3d object detection network for autonomous driving," in *CVPR*, 2017. 1, 2
- [3] B. Yang, W. Luo, and R. Urtasun, "Pixor: Real-time 3d object detection from point clouds," in *CVPR*, 2018. 1, 2, 4, 9
- [4] C. R. Qi, W. Liu, C. Wu, H. Su, and L. J. Guibas, "Frustum pointnets for 3d object detection from rgb-d data," in *CVPR*, 2018. 1
- [5] A. H. Lang, S. Vora, H. Caesar, L. Zhou, J. Yang, and O. Beijbom, "Pointpillars: Fast encoders for object detection from point clouds," in *CVPR*, 2019. 1
- [6] S. Shi, C. Guo, L. Jiang, Z. Wang, J. Shi, X. Wang, and H. Li, "Pv-rcnn: Point-voxel feature set abstraction for 3d object detection," in *CVPR*, 2020. 1, 2
- [7] J.-R. Chang and Y.-S. Chen, "Pyramid stereo matching network," in *CVPR*, 2018. 2, 4
- [8] A. Kendall, H. Martirosyan, S. Dasgupta, P. Henry, R. Kennedy, A. Bachrach, and A. Bry, "End-to-end learning of geometry and context for deep stereo regression," in *ICCV*, 2017. 2
- [9] Y. Chen, S. Liu, X. Shen, and J. Jia, "Dsgn: Deep stereo geometry network for 3d object detection," in *CVPR*, 2020. 1, 2, 3, 5, 6
- [10] Y. You, Y. Wang, W.-L. Chao, D. Garg, G. Pleiss, B. Hariharan, M. Campbell, and K. Q. Weinberger, "Pseudo-lidar++: Accurate depth for 3d object detection in autonomous driving," in *ICLR*, 2020. 1, 2, 3, 5, 6
- [11] M. Liang, B. Yang, Y. Chen, R. Hu, and R. Urtasun, "Multi-task multi-sensor fusion for 3d object detection," in *CVPR*, 2019. 1, 2
- [12] X. Chen, K. Kundu, Z. Zhang, H. Ma, S. Fidler, and R. Urtasun, "Monocular 3d object detection for autonomous driving," in *CVPR*, 2016. 1, 2
- [13] B. Xu and Z. Chen, "Multi-level fusion based 3d object detection from monocular images," in *CVPR*, 2018. 1, 2, 6
- [14] Y. Wang, W.-L. Chao, D. Garg, B. Hariharan, M. Campbell, and K. Q. Weinberger, "Pseudo-lidar from visual depth estimation: Bridging the gap in 3d object detection for autonomous driving," in *CVPR*, 2019. 1, 2, 3, 5, 6
- [15] D. Garg, Y. Wang, B. Hariharan, M. Campbell, K. Q. Weinberger, and W.-L. Chao, "Wasserstein distances for stereo disparity estimation," in *NeurIPS*, 2020. 1, 2, 3, 5, 6
- [16] C. Li, J. Ku, and S. L. Waslander, "Confidence guided stereo 3d object detection with split depth estimation," *IROS*, 2020. 1, 2, 3
- [17] A. Geiger, P. Lenz, and R. Urtasun, "Are we ready for autonomous driving? the kitti vision benchmark suite," in *CVPR*, 2012. 2
- [18] D. Scharstein and R. Szeliski, "A taxonomy and evaluation of dense two-frame stereo correspondence algorithms," *IJCV*, 2002. 2
- [19] J. Zbontar and Y. LeCun, "Stereo matching by training a convolutional neural network to compare image patches," *JMLR*, 2016. 2
- [20] W. Luo, A. G. Schwing, and R. Urtasun, "Efficient deep learning for stereo matching," in *CVPR*, 2016. 2
- [21] Y. Zhou and O. Tuzel, "Voxelnet: End-to-end learning for point cloud based 3d object detection," in *CVPR*, 2018. 2
- [22] B. Yang, M. Liang, and R. Urtasun, "Hdnet: Exploiting hd maps for 3d object detection," in *CoRL*, 2018. 2
- [23] M. Liang, B. Yang, S. Wang, and R. Urtasun, "Deep continuous fusion for multi-sensor 3d object detection," in *ECCV*, 2018. 2
- [24] C. R. Qi, L. Yi, H. Su, and L. J. Guibas, "Pointnet++: Deep hierarchical feature learning on point sets in a metric space," in *NIPS*, 2017. 2
- [25] S. Wang, S. Suo, W.-C. M. A. Pokrovsky, and R. Urtasun, "Deep parametric continuous convolutional neural networks," in *CVPR*, 2018. 2
- [26] S. Shi, X. Wang, and H. Li, "Pointcrnn: 3d object proposal generation and detection from point cloud," in *CVPR*, 2019. 2
- [27] Z. Liu, H. Tang, Y. Lin, and S. Han, "Point-voxel cnn for efficient 3d deep learning," in *NeurIPS*, 2019. 2
- [28] K. He, G. Gkioxari, P. Dollár, and R. Girshick, "Mask r-cnn," in *ICCV*, 2017. 2
- [29] T.-Y. Lin, P. Dollár, R. B. Girshick, K. He, B. Hariharan, and S. J. Belongie, "Feature pyramid networks for object detection," in *CVPR*, 2017. 2, 4, 5
- [30] S. Ren, K. He, R. Girshick, and J. Sun, "Faster r-cnn: Towards real-time object detection with region proposal networks," in *NIPS*, 2015. 2
- [31] F. Chabot, M. Chaouch, J. Rabarisoa, C. Teulière, and T. Chateau, "Deep manta: A coarse-to-fine many-task network for joint 2d and 3d vehicle analysis from monocular image," in *CVPR*, 2017. 2
- [32] X. Chen, K. Kundu, Y. Zhu, A. G. Berneshawi, H. Ma, S. Fidler, and R. Urtasun, "3d object proposals for accurate object class detection," in *NIPS*, 2015. 2, 5, 6
- [33] X. Chen, K. Kundu, Y. Zhu, H. Ma, S. Fidler, and R. Urtasun, "3d object proposals using stereo imagery for accurate object class detection," *TPAMI*, vol. 40, no. 5, pp. 1259–1272, 2018. 2
- [34] A. Mousavian, D. Anguelov, J. Flynn, and J. Košecká, "3d bounding box estimation using deep learning and geometry," in *CVPR*, 2017. 2
- [35] B. Li, W. Ouyang, L. Sheng, X. Zeng, and X. Wang, "Gs3d: An efficient 3d object detection framework for autonomous driving," in *CVPR*, 2019. 2
- [36] C. C. Pham and J. W. Jeon, "Robust object proposals re-ranking for object detection in autonomous driving using convolutional neural networks," *Signal Processing: Image Communication*, vol. 53, pp. 110–122, 2017. 2
- [37] Y. Xiang, W. Choi, Y. Lin, and S. Savarese, "Data-driven 3d voxel patterns for object category recognition," in *CVPR*, 2015. 2
- [38] —, "Subcategory-aware convolutional neural networks for object proposals and detection," in *WACV*, 2017. 2
- [39] T. Roddick, A. Kendall, and R. Cipolla, "Orthographic feature transform for monocular 3d object detection," in *BMVC*, 2019. 2, 3
- [40] A. D. Pon, J. Ku, C. Li, and S. L. Waslander, "Object-centric stereo matching for 3d object detection," in *ICRA*, 2020. 2, 5, 6
- [41] J. Sun, L. Chen, Y. Xie, S. Zhang, Q. Jiang, X. Zhou, and H. Bao, "Disp r-cnn: Stereo 3d object detection via shape prior guided instance disparity estimation," in *CVPR*, 2020. 2, 5, 6
- [42] R. Qian, D. Garg, Y. Wang, Y. You, S. Belongie, B. Hariharan, M. Campbell, K. Q. Weinberger, and W.-L. Chao, "End-to-end pseudo-lidar for image-based 3d object detection," in *CVPR*, 2020. 2, 3, 5, 6
- [43] A. Kar, C. Häne, and J. Malik, "Learning a multi-view stereo machine," in *NeurIPS*, 2017. 3
- [44] K. He, X. Zhang, S. Ren, and J. Sun, "Deep residual learning for image recognition," in *CVPR*, 2016. 5, 9
- [45] P. Li, X. Chen, and S. Shen, "Stereo r-cnn based 3d object detection for autonomous driving," in *CVPR*, 2019. 5, 6
- [46] H. Königshof, N. O. Salscheider, and C. Stiller, "Realtime 3d object detection for automated driving using stereo vision and semantic information," in *ITSC*, 2019. 5
- [47] Z. Xu, W. Zhang, X. Ye, X. Tan, W. Yang, S. Wen, E. Ding, A. Meng, and L. Huang, "Zoomnet: Part-aware adaptive zooming neural network for 3d object detection," in *AAAI*, 2020. 5, 6



TABLE V

PLUMENET ARCHITECTURE.  $s$  AND  $d$  ARE STRIDE AND DILATION.  $H$  AND  $W$  ARE IMAGE HEIGHT AND WIDTH.  $X$ ,  $Y$  AND  $Z$  ARE FEATURE VOLUME WIDTH, HEIGHT AND DEPTH LAYER  $\{1,2,3,4\}$  ARE CASCADES OF BASIC RESIDUAL LAYERS [44].

PLUMENet-Small		PLUMENet-Middle		PLUMENet-Large		
Layer	Setting	Output Dimension	Setting	Output Dimension	Setting	Output Dimension
Image		$3 \times H \times W$		$3 \times H \times W$		$3 \times H \times W$
<b>Stereo Image Network: Feature Encoder</b>						
conv0	$(3 \times 3) \times 3$	$32 \times H \times W$	$(3 \times 3) \times 3$	$32 \times H \times W$	$(3 \times 3) \times 3$	$32 \times H \times W$
maxpool0	$(3 \times 3) \times 1, s=2$	$8 \times \frac{1}{2}H \times \frac{1}{2}W$	$(3 \times 3) \times 1, s=2$	$32 \times \frac{1}{2}H \times \frac{1}{2}W$	$(3 \times 3) \times 1, s=2$	$32 \times \frac{1}{2}H \times \frac{1}{2}W$
layer1	$(3 \times 3) \times 3$	$8 \times \frac{1}{2}H \times \frac{1}{2}W$	$(3 \times 3) \times 3$	$32 \times \frac{1}{2}H \times \frac{1}{2}W$	$(3 \times 3) \times 3$	$32 \times \frac{1}{2}H \times \frac{1}{2}W$
layer2	$(3 \times 3) \times 6, s=2$	$16 \times \frac{1}{4}H \times \frac{1}{4}W$	$(3 \times 3) \times 6, s=2$	$64 \times \frac{1}{4}H \times \frac{1}{4}W$	$(3 \times 3) \times 6, s=2$	$64 \times \frac{1}{4}H \times \frac{1}{4}W$
layer3	$(3 \times 3) \times 2$	$32 \times \frac{1}{4}H \times \frac{1}{4}W$	$(3 \times 3) \times 2$	$128 \times \frac{1}{4}H \times \frac{1}{4}W$	$(3 \times 3) \times 6$	$128 \times \frac{1}{4}H \times \frac{1}{4}W$
layer4	$(3 \times 3) \times 2, d=2$	$32 \times \frac{1}{4}H \times \frac{1}{4}W$	$(3 \times 3) \times 2, d=2$	$128 \times \frac{1}{4}H \times \frac{1}{4}W$	$(3 \times 3) \times 6, d=2$	$128 \times \frac{1}{4}H \times \frac{1}{4}W$
branch1	$(64 \times 64)$ avgpool $(3 \times 3)$ conv upsample	$8 \times \frac{1}{4}H \times \frac{1}{4}W$	$(64 \times 64)$ avgpool $(3 \times 3)$ conv upsample	$32 \times \frac{1}{4}H \times \frac{1}{4}W$	$(64 \times 64)$ avgpool $(3 \times 3)$ conv upsample	$32 \times \frac{1}{4}H \times \frac{1}{4}W$
branch2	$(32 \times 32)$ avgpool $(3 \times 3)$ conv upsample	$8 \times \frac{1}{4}H \times \frac{1}{4}W$	$(32 \times 32)$ avgpool $(3 \times 3)$ conv upsample	$32 \times \frac{1}{4}H \times \frac{1}{4}W$	$(32 \times 32)$ avgpool $(3 \times 3)$ conv upsample	$32 \times \frac{1}{4}H \times \frac{1}{4}W$
branch3	$(16 \times 16)$ avgpool $(3 \times 3)$ conv upsample	$8 \times \frac{1}{4}H \times \frac{1}{4}W$	$(16 \times 16)$ avgpool $(3 \times 3)$ conv upsample	$32 \times \frac{1}{4}H \times \frac{1}{4}W$	$(16 \times 16)$ avgpool $(3 \times 3)$ conv upsample	$32 \times \frac{1}{4}H \times \frac{1}{4}W$
branch4	$(8 \times 8)$ avgpool $(3 \times 3)$ conv upsample	$8 \times \frac{1}{4}H \times \frac{1}{4}W$	$(8 \times 8)$ avgpool $(3 \times 3)$ conv upsample	$32 \times \frac{1}{4}H \times \frac{1}{4}W$	$(8 \times 8)$ avgpool $(3 \times 3)$ conv upsample	$32 \times \frac{1}{4}H \times \frac{1}{4}W$
concat(layer $\{2,4\}$ , branch $\{1,2,3,4\}$ )		$80 \times \frac{1}{4}H \times \frac{1}{4}W$		$320 \times \frac{1}{4}H \times \frac{1}{4}W$		$320 \times \frac{1}{4}H \times \frac{1}{4}W$
conv1	$(3 \times 3) \times 1$	$32 \times \frac{1}{4}H \times \frac{1}{4}W$	$(3 \times 3) \times 1$	$128 \times \frac{1}{4}H \times \frac{1}{4}W$	$(3 \times 3) \times 1$	$128 \times \frac{1}{4}H \times \frac{1}{4}W$
conv2	$(1 \times 1) \times 1$	$8 \times \frac{1}{4}H \times \frac{1}{4}W$	$(1 \times 1) \times 1$	$32 \times \frac{1}{4}H \times \frac{1}{4}W$	$(1 \times 1) \times 1$	$32 \times \frac{1}{4}H \times \frac{1}{4}W$
<b>Stereo Image Network: Feature Decoder</b>						
fpn_conv2	input: conv1 $(1 \times 1) \times 1$	$32 \times \frac{1}{4}H \times \frac{1}{4}W$	input: conv1 $(1 \times 1) \times 1$	$64 \times \frac{1}{4}H \times \frac{1}{4}W$	input: conv1 $(1 \times 1) \times 1$	$96 \times \frac{1}{4}H \times \frac{1}{4}W$
fpn_conv2_up	$(3 \times 3)$ conv upsample $\times 2$	$32 \times H \times W$	$(3 \times 3)$ conv upsample $\times 2$	$64 \times H \times W$	$(3 \times 3)$ conv upsample $\times 2$	$96 \times H \times W$
fpn_conv1	input: layer1 $(1 \times 1)$ conv upsample fpn_conv2 sum	$32 \times \frac{1}{2}H \times \frac{1}{2}W$	input: layer1 $(1 \times 1)$ conv upsample fpn_conv2 sum	$64 \times \frac{1}{2}H \times \frac{1}{2}W$	input: layer1 $(1 \times 1)$ conv upsample fpn_conv2 sum	$96 \times \frac{1}{2}H \times \frac{1}{2}W$
fpn_conv1_up	$(3 \times 3)$ conv upsample $\times 1$	$32 \times H \times W$	$(3 \times 3)$ conv upsample $\times 1$	$64 \times H \times W$	$(3 \times 3)$ conv upsample $\times 1$	$96 \times H \times W$
fpn_conv0	input: conv0 $(1 \times 1)$ conv upsample fpn_conv1 sum	$32 \times H \times W$	input: conv0 $(1 \times 1)$ conv upsample fpn_conv1 sum	$64 \times H \times W$	input: conv0 $(1 \times 1)$ conv upsample fpn_conv1 sum	$96 \times H \times W$
fpn_conv0_up	$(3 \times 3) \times 1$	$32 \times H \times W$	$(3 \times 3) \times 1$	$64 \times H \times W$	$(3 \times 3) \times 1$	$96 \times H \times W$
sum(fpn_conv $\{0,1,2\}$ _up)		$32 \times H \times W$		$64 \times H \times W$		$96 \times H \times W$
dropout	p=0.2	$32 \times H \times W$	p=0.2	$64 \times H \times W$	p=0.2	$96 \times H \times W$
fpn_conv	$(3 \times 3) \times 1$	$32 \times H \times W$	$(3 \times 3) \times 1$	$32 \times H \times W$	$(3 \times 3) \times 1$	$32 \times H \times W$
<b>3D-BEV Network</b>						
Pseudo-LiDAR Feature Volume		$64 \times X \times Y \times Z$		$64 \times X \times Y \times Z$		$64 \times X \times Y \times Z$
3dconv0	$(3 \times 3 \times 3) \times 2$	$12 \times X \times Y \times Z$	$(3 \times 3 \times 3) \times 2$	$32 \times X \times Y \times Z$	$(3 \times 3 \times 3) \times 2$	$48 \times X \times Y \times Z$
reshape 3D feature volume to 2D		$(12 \times Y) \times X \times Z$		$(32 \times Y) \times X \times Z$		$(48 \times Y) \times X \times Z$
bev_conv0	$(3 \times 3) \times 2$	$96 \times X \times Z$	$(3 \times 3) \times 2$	$160 \times X \times Z$	$(3 \times 3) \times 2$	$256 \times X \times Z$
bev_conv1	$(3 \times 3) \times 2$ add bev_conv0	$96 \times X \times Z$	$(3 \times 3) \times 2$ add bev_conv0	$160 \times X \times Z$	$(3 \times 3) \times 2$ add bev_conv0	$256 \times X \times Z$
bev_conv2	$(3 \times 3) \times 2, s=2$	$192 \times \frac{1}{2}X \times \frac{1}{2}Z$	$(3 \times 3) \times 2, s=2$	$320 \times \frac{1}{2}X \times \frac{1}{2}Z$	$(3 \times 3) \times 2, s=2$	$512 \times \frac{1}{2}X \times \frac{1}{2}Z$
bev_conv3	$(3 \times 3) \times 2, s=2$	$192 \times \frac{1}{4}X \times \frac{1}{4}Z$	$(3 \times 3) \times 2, s=2$	$320 \times \frac{1}{4}X \times \frac{1}{4}Z$	$(3 \times 3) \times 2, s=2$	$512 \times \frac{1}{4}X \times \frac{1}{4}Z$
bev_deconv4	$(3 \times 3) \times 2$ deconv add bev_conv2	$192 \times \frac{1}{2}X \times \frac{1}{2}Z$	$(3 \times 3) \times 2$ deconv add bev_conv2	$320 \times \frac{1}{2}X \times \frac{1}{2}Z$	$(3 \times 3) \times 2$ deconv add bev_conv2	$512 \times \frac{1}{2}X \times \frac{1}{2}Z$
bev_deconv5	$(3 \times 3) \times 2$ deconv	$96 \times X \times Z$	$(3 \times 3) \times 2$ deconv	$160 \times X \times Z$	$(3 \times 3) \times 2$ deconv	$256 \times X \times Z$
<b>Occupancy Header</b>						
conv3	$(3 \times 3) \times 1$	$48 \times X \times Z$	$(3 \times 3) \times 1$	$80 \times X \times Z$	$(3 \times 3) \times 1$	$128 \times X \times Z$
conv4	$(3 \times 3) \times 1$	$Y \times X \times Z$	$(3 \times 3) \times 1$	$Y \times X \times Z$	$(3 \times 3) \times 1$	$Y \times X \times Z$

## VI. APPENDIX: MODEL ARCHITECTURE

We provide PLUMENet small, middle and large architectures in Table V, which consist of stereo image network, 3D-BEV network and occupancy header. Both the occupancy header and detection header take as input the bev\_conv5 in Table V. The detection header consists of five blocks of layers. We show the number of layers and the output channels of each block in Table VI. We refer readers to PIXOR [3] for more details of the detection header.

TABLE VI  
CONFIGURATIONS OF THE DETECTION HEADER.

	number of layers	number of channels
Small	2, 3, 6, 6, 3	32, 96, 128, 192, 192
Middle	2, 3, 6, 6, 3	32, 96, 192, 256, 384
Large	3, 3, 6, 6, 3	48, 128, 192, 256, 384